17

SEM Analysis of Precipitation Process in Alloys

Maribel L. Saucedo-Muñoz,
Victor M. Lopez-Hirata and Hector J. Dorantes-Rosales
Instituto Politecnico Nacional (ESIQIE),
Mexico

1. Introduction

The microstructural characterization of the precipitation process in alloys is a very important aspect in order to understand the formation mechanism and growth kinetics of precipitated phases during its heating because of either the heat treating process or the operation-in-service conditions. Additionally, the microstructure control is a key point to know the degree of hardening after heat treating of the alloys and to assess their mechanical properties after a prolonged exposure at high temperature during the operation of an industrial component. There are different characterization techniques for microstructure; however, the use of the scanning electron microscopy, SEM, has been very popular for the microstructural observation and it has become a power tool for characterization of the phase transformations. Besides, the application of energy-dispersed-spectra, EDS-SEM system to the microstructural characterization has permitted to know not only the morphology of phases, sizes, distribution and then growth kinetics, but also their chemical composition and thus element distribution of the formed phases. Thus this chapter shows the application of SEM-EDS system to the characterization of microstructural of precipitation process in different alloy systems such as Fe-Ni-Al alloy, austenitic stainless steels and Mg-Zn-Al alloy.

2. Precipitation in alloys

Phase separation in alloys usually consists of the formation of a supersaturated solid solution by heating the alloy at temperatures higher than the equilibrium solvus line and subsequently quenched rapidly. This supersaturated solid solution can usually be separated in two or more phases as a result of the isothermal aging at temperatures lower than that of equilibrium. Phase separation can mainly take place by two mechanisms, nucleation and growth, and spinodal decomposition (Porter, 2009). The former mechanism consists of the formation of a stable nucleus with a nucleation barrier to overcome and it is characterized by an incubation period. In contrast, the latter one is initiated by the spontaneous formation and subsequent growth of coherent composition fluctuations. The formation of fine second-phase dispersion in a matrix promotes its hardening, known as precipitation hardening. If the aging of alloys continues, it is expected that larger precipitates will grow at the expense of smaller ones which dissolve again given rise to a change in the precipitate size distribution (Kostorz, 2005).

2.1 Coarsening process in Fe-Ni-Al alloys

The precipitation of the β´phase is important for strengthening at high temperatures in different engineering ferritic alloys such as, PH stainless steels, nitralloy, Fe-Cr-Ni-Al based alloys, etc. These alloys are used in industrial components which require good mechanical strength and oxidation resistance at high temperatures. The β´phase is an ordered phase of the B2 type crystalline structure (Sauthoff, 2004). The coarsening resistance of precipitates is a key factor to keep the high strength at high temperatures in this type of alloys. An alternative to have a good coarsening resistance, it is to have a low value of lattice misfit which maintains a coherent interface between the precipitate and matrix (Kostorz, 2005). Thus, this section shows the effect of structural and morphological characteristics of the β´ precipitates on the coarsening behavior during the isothermal aging of an Fe-10Ni-15Al alloy.

2.1.1 Experimental details

An Fe-10Ni-15Al alloy (wt. %) was melted using pure metallic elements in an electrical furnace under an argon atmosphere. The ingot of 30 x 10 x 10 mm was encapsulated in a quartz tube with argon gas and then homogenized at 1100 °C for one week. Specimens were solution treated at 1100 °C for 1 h and subsequently aged at temperatures of 750, 850 and 920 °C for times from 0.25 to 750 h. These samples were also observed with a SEM analysis with EDS detector at 20 kV. Vickers hardness was tested for the aged specimens using a load of 100 g.

2.1.2 Microstructural evolution of coarsening

SEM micrographs of precipitates are shown for the sample aged at 750 and 920 °C for different times in Figs. 1 (a-c) and (d-f), respectively. The shape of the β´ precipitates was round without any preferential alignment for the aging at 750 °C up to 75 h and 920 °C up to 0.5 h, Figs 1 (a). A further aging changed the shape of the β´ precipitates to cuboids with a preferential alignment on the <100> directions of the ferritic α phase, Figs. 1 (c-e). A prolonged aging at 920 °C promoted the change of shape to rectangular plates also aligned in the <100> directions, Fig. 1 (f). The volume percentage of precipitation was determined to be about 30, 25 and 20 % for the samples aged at 750, 850 and 920 °C, respectively.

2.1.3 Growth kinetics of coarsening

The variation of the β´ precipitates size expressed as r^3-r_o^3 with aging time for the sample aged at 750, 850 and 920 °C is shown in Fig. 2. It can be noticed that the experimental data fit to a straight line for each temperature. Thus the growth kinetics of coarsening followed the behavior predicted by the Lifshitz-Slyozov-Wagner (LSW) theory for coarsening controlled by volume diffusion. This fact shows a good agreement with the modified theory for the diffusion-controlled coarsening in ternary alloys (Kostorz, 2005) which predicts that growth kinetics is similar to that of LSW theory. The size distribution of precipitates is shown in Figs. 3 (a-c) for the sample aged at 750, 850 and 920 °C for 200 h, respectively. It can be seen that the size distribution is broader and lower than that predicted by the LSW theory because of the high volume fraction of precipitates, which has been reported in the coarsening process of several alloy systems. It has been observed that the growth or

shrinkage rate of an individual particle depends not only on its normalized radii but also on its local environment. That is, a particle surrounded by several larger particles will grow slower, or shrink faster, than a particle of the same size whose neighbors are smaller. Thus, as the volume fraction increased, the particle size distribution widened increasing the coarsening rate at the same time. It was also observed that the higher aging temperature, the faster coarsening kinetics of the β´ precipitates because of the increase in volume diffusion (Ratke & Vorhees, 2002).

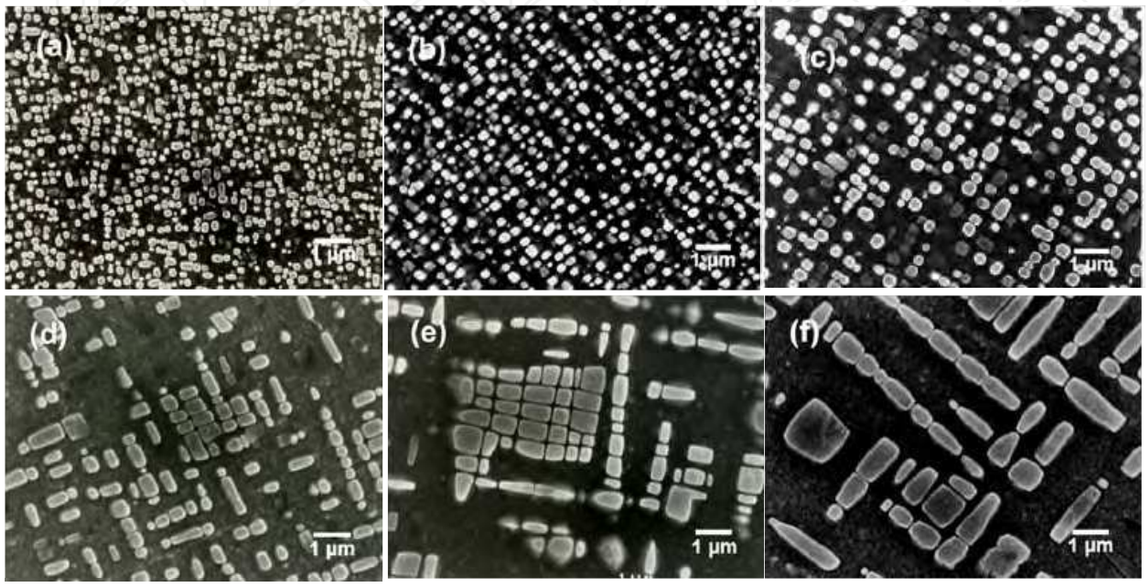

Fig. 1. SEM micrographs for the Fe-10Ni-15Al alloy aged at 750 °C for (a) 75, (b) 250, and (c) 500 h, and at 920 °C for (d) 25, (e) 100 and (f) 200 h.

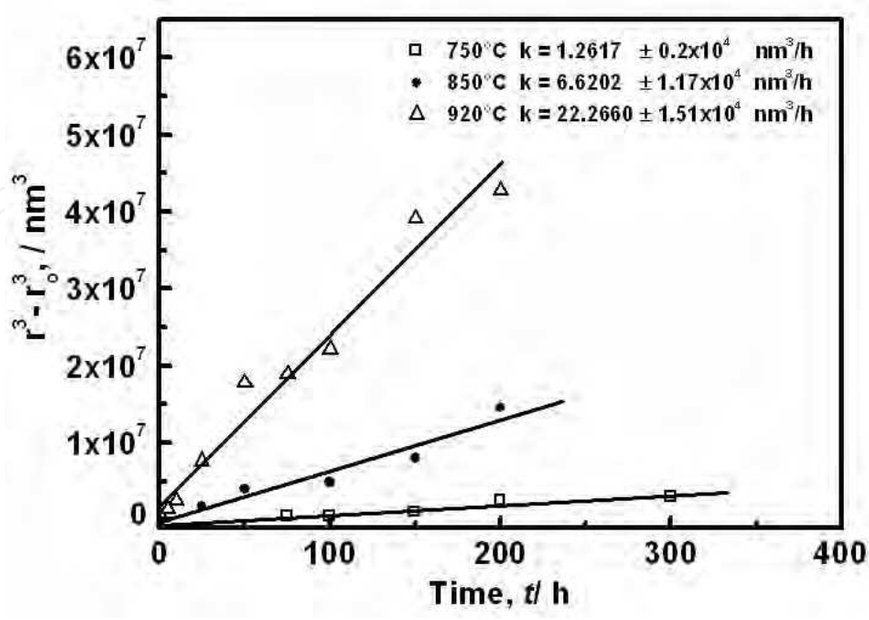

Fig. 2. Plot of r^3-r_o^3 vs. aging time for the Fe-10Ni-15Al alloy aged at 750, 850 and 920 °C.

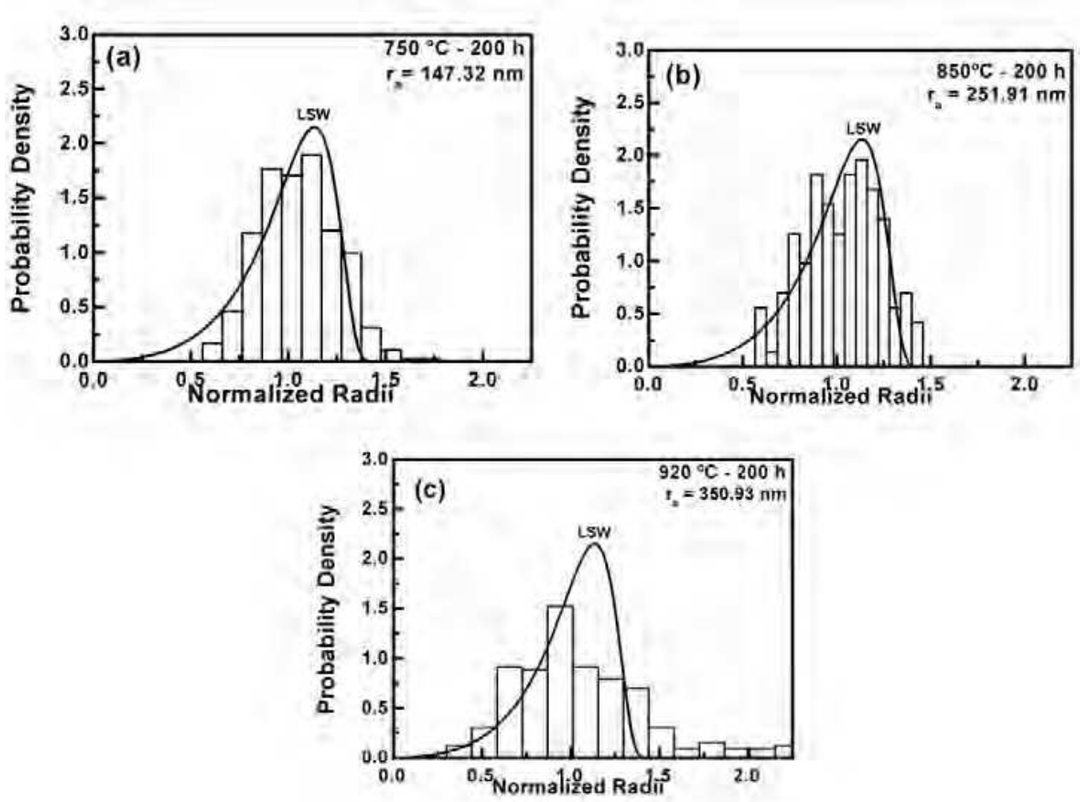

Fig. 3. Size distribution of precipitates for the Fe-10Ni-15Al alloy aged at (a) 750, (b) 850 and (c) 920 °C for 200 h.

2.1.4 Hardening behavior

Figure 4 shows the aging curves for the sample aged at 750 and 920 °C. A higher hardness can be noticed in the sample aged at 920 °C. This can be attributed to the morphology and alignment of β´ precipitates. That is, they are cuboids aligned in the <100> crystallographic directions of the ferritic matrix. A similar hardening behavior was observed in Fe-Ni-Al alloys aged at lower temperatures, 500 °C (Soriano-Vargas et al. 2010, Cayetano-Castro et al. 2008). In contrast, the precipitates are rounded particles without any preferential crystallographic alignment for aging at 750 °C up to 75 h. Besides, the size of β´ precipitates is much smaller than that of the sample aged at 920 °C. It can also be observed that the hardness peak is first reached in the aging at 750 °C than that at 920 °C. Additionally, the overaging started first for the aging at 750 °C. Besides, the hardness is almost the same value for prolonged aging at both temperatures. All the above facts suggest that even the coarsening process at 920 °C is the fastest one, the cuboid morphology and alignment of β´ precipitates causes a higher hardness peak and a slower overaging process than those corresponding at 750 °C.

In summary, the aging process of the Fe-10Ni-15Al alloy promoted the precipitation of the β´(Fe(NiAl)) precipitates with the B2 type crystalline structure. The morphology of β´ precipitates was rounded at the early stages of aging and then it changed to cuboids aligned in the <100> directions of the ferritic matrix. A prolonged aging caused the formation of

rectangular plates also aligned in this direction. The coarsening process followed the growth kinetics predicted by the LSW theory. Nevertheless, the hardness peak was higher and the overaging process occurred later in the sample aged at 920 °C than those of the sample aged at 750 °C. This behavior can be attributed to the fast formation of cuboid morphology and alignment in the <100> direction due to the higher lattice misfit between the ferritic matrix and β´ precipitate at this aging temperature.

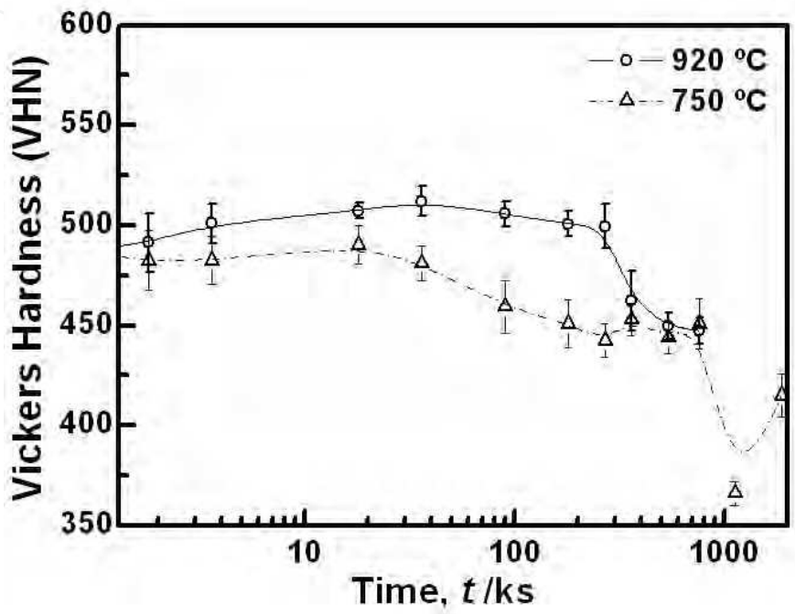

Fig. 4. Aging curves for the Fe-10Ni-15Al alloy aged at 750 and 920 °C.

2.2 Precipitation in austenitic stainless steels

The austenitic stainless steels are construction materials for key corrosion-resistant equipment in most of the major industries, particularly in the chemical, petroleum, and nuclear power industries (Marshal, 1984). These steels are iron alloys containing a minimum of approximately 12 % chromium. This content of chromium allows the formation of the passive film, which is self-healing in a wide variety of environments. Nitrogen as an alloying element in iron-based alloys is known since the beginning of the last century having been profoundly studied during the last three decades (Nakajima et al., 1996). Nevertheless, nitrogen steels are now not widely used. The reason for the comparatively narrow industrial application lies in the old customer skepticism in relation to nitrogen as an element causing brittleness in ferritic steels, some technical problems involved with nitrogen into steel, and the insufficient knowledge of the physical nature of nitrogen in iron and its alloys. In the case of austenitic stainless steels, the main driving force in the development of nitrogen-containing steels is due to the higher yield and tensile strengths achieved, compared with conventionally-processed austenitic stainless steels without sacrificing toughness. Nitrogen stainless steels have yield and tensile strengths as much as 200-350 % of the AISI 300 series steels. It is also important to notice that, in contrast to carbon, nitrogen-containing austenitic stainless steels retain high fracture toughness at low temperatures. Therefore, the higher mechanical properties of nitrogen-containing austenitic

stainless steels have made very attractive its application in the power-generation industry, shipbuilding, railways, cryogenic process, chemical equipment, pressure vessels and nuclear industries (Nakajima et al. 1989). These stainless steels are also susceptible to the precipitation of different phases because of the aging for long exposition at high temperatures or during continuous cooling after a welding process. Therefore, it is important to evaluate the degree of microstructural degradation due to the precipitation phenomenon which may affect the cryogenic toughness in this type of steels. In this section, three types of austenitic stainless steels, JJ1, JN1 and JK2 developed for applications to the superconducting magnets of fusion experimental reactor by JAERI, were selected to study the microstructure evolution during isothermal aging.

2.2.1 Experimental details

Materials used in this work were forged-steel plates of 200 mm thick and their chemical compositions are shown in Table 1. The solution treatment of JN1, and JJ1 and JK2 was carried out at 1075 and 1050 °C, respectively, for 1 hour under an argon atmosphere, and then water-quenched. The aging temperatures and times were 600, 700, 800 and 900 °C and from 10 to 1000 minutes, respectively. The aged samples were prepared metallographically and etched with Vilella´s reagent. The precipitates in the aged samples were extracted electrolitically by dissolution of the austenitic matrix in a solution of 10 vol. %HCl-CH_3OH at 4 volts. The X-ray diffraction pattern of extracted precipitates was measured in a diffractometer using Kα Cu radiation. The SEM/EDX microanalysis of precipitates was also conducted using the extraction replica technique.

Material	C	Si	Mn	Ni	Cr	Al	N	Mo
JN1	0.040	0.97	3.88	15.07	24.32	0.023	0.32	---
JJ1	0.025	0.48	10.13	11.79	12.01	---	0.236	4.94
JK2	0.05	0.39	21.27	9.15	12.97	---	0.247	0.97

Table 1. Chemical composition (wt.%) of materials.

2.2.2 Microstructural evolution

An intergranular precipitation can be observed for all cases. The highest and lowest volume fraction of intergranular precipitates corresponded to the aged JN1 and JK2 steels, respectively, Figs. 5 (a-b) and (e-f). The presence of an intergranular cellular precipitation of Cr_2N was observed to occur in the JN1 steel sample aged at 900 °C. No intergranular precipitation was practically detected for the JK2 steel aged at 700 °C. The intragranular precipitates can be classified into two types: cellular or discontinuous precipitation and plate-like precipitates, which have a preferred alignment with the austenitic matrix. The morphology of cellular precipitates is similar to that of pearlite in carbon-steels, Fig. 6. The formation of this lamellar microstructure initiated at grain boundaries and grew into the austenite γ matrix, according to the following reaction:

$$\gamma \rightarrow \gamma + Cr_2N \quad (1)$$

The volume fraction of the discontinuous precipitation increased with time and the maximum value was determined by the point-count grid method, to be about 0.04. This value seems to be reasonable, since a volume fraction of 0.1 was reported in an austenitic stainless steel containing 0.42 % N, after a long heat treatment (Kikuchi et al., 1991). Some small intragranular precipitates were present in the JN1 and JJ1 steels aged at 700 and 800 °C for 5 h, Figs. 5 (a-d). The volume fraction of intragranular precipitates for the aged JJ1 steel was slightly higher than that of the aged JN1 steel. This tendency became higher by increasing the aging temperature. Almost no intragranular precipitation was observed in the aged JK2 steel. The precipitation of particles was also observed to occur on twin boundaries for the aged JN1 steel. The X-ray diffraction patterns of residues extracted from the JN1, JJ1 and JK2 steels aged at 700 and 800 °C for 5 h are shown in Fig. 7. The extracted precipitates of the JN1 steel, aged at 700 and 800 °C for 5 h, were identified as $Cr_{23}C_6$ and Cr_2N. The Cr_2N and $Cr_{23}C_6$ phases were also detected in the aged JJ1 steel. Besides, the presence of the (Fe_2Mo) η phase was also noted in the samples aged at 800 and 900 °C. The precipitated particles of JK2 steel were mainly composed of $Cr_{23}C_6$. According to the chemical composition, shown in Table 1, the JN1 steel has the highest and lowest contents of interstitial solutes (C and N), and Mn, respectively. This suggests that the highest volume fraction of precipitation for carbides and nitrides must have occurred in this steel. In contrast, the JK2 steel has an interstitial solute content lower than that of the JN1 steel, but it has the highest content of manganese, which maintains nitrogen in solid solution, avoiding its precipitation. That is, it is only expected the precipitation of carbides for this steel. This fact showed a good agreement with the above results.

2.2.3 Precipitation kinetics

All the above results are summarized in the Time-Temperature-Precipitation (TTP) diagrams of JN1, JJ1 and JK2 steels, as shown in Figs. 8 (a-c), respectively. In general, it can be noticed that the kinetics of precipitation for JN1 steel is faster than that of JJ1 steel, because of its higher interstitial solute content. The TTP diagrams show that the intergranular precipitation of $Cr_{23}C_6$ and Cr_2N preceded to the intragranular precipitation of Cr_2N, and Cr_2N and η phase in JN1 and JJ1 steels, respectively.

2.2.4 Fracture toughness

In contrast, Figs. 9 (a), (b) and (c) show the plots of CVN fracture energy at -196 °C versus aging time for the JN1, JJ1 and JK2 steels aged at 700, 800 and 900 °C, respectively. All the steels showed a monotonotic decrease in the CVN fracture energy with aging time at the three temperatures. It is also evident that the drop of fracture toughness of JN1 steel is always faster than that of JJ1 steel. The fastest drop of fracture toughness occurred in the JN1 steel samples aged at 900 °C. This fact may be attributed to the higher content of C and N in JN1 steel, which can lead to faster kinetics in intergranular precipitation during the aging process, as discussed in a later section. The CVN fracture energy of solution treated JK2 steel was lower than that corresponding to the other two steels. The lowest decrease in the CVN fracture energy was for the aged JK2 steel. Furthermore, the JK2 steel, aged at 900 °C, showed almost no change in the fracture energy with time. All the JN1, JJ1 and JK2 steels fractured in a ductile manner in the solution treated condition. Intergranular facets were found in all the aged samples, although the area fraction of intergranular facets to ductile

surface was strongly dependent on aging conditions. The fraction of intergranular brittle fracture increased with time and temperature, and it seemed consistent with the CVN fracture energy value. Nevertheless, the fracture surface of the JK2 steel, aged at 900 °C, showed almost a complete ductile- fracture mode. These results are in agreement with the fracture mode observed in the tested SP test specimens.

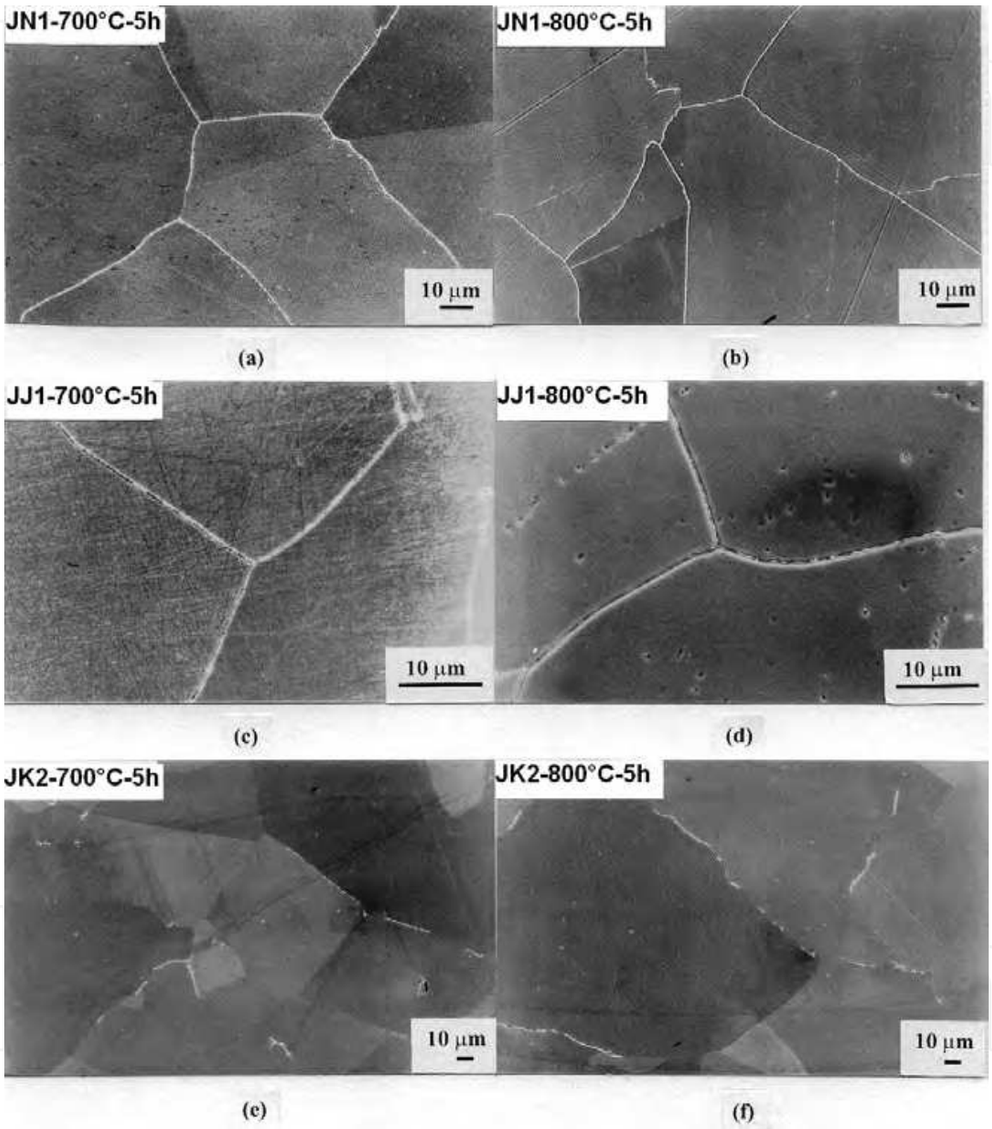

Fig. 5. SEM micrographs of JN1, JJ1 and JK2 steels aged at 700 and 800 °C for 5 h.

In summary, the highest and lowest degradation in toughness for JN1 and JK2 steel, respectively, is associated with the volume fraction of intergranular precipitation formed during the thermal aging. An abundant presence of intergranular precipitates was reported to causes the reduction of cohesive strength of grain boundaries (Saucedo et al., 2001). This is also confirmed by the increase in intergranular brittle fracture as the thermal aging progresses.

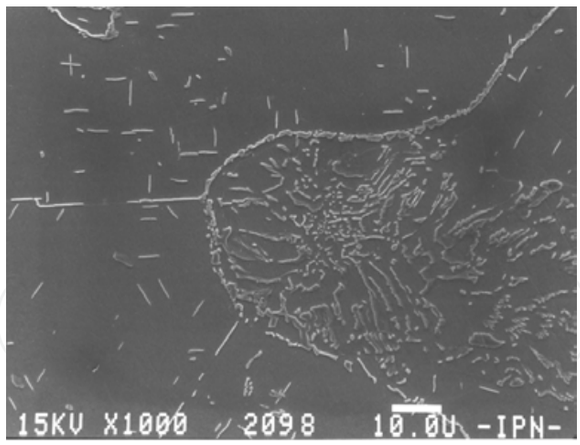

Fig. 6. SEM micrograph of the cellular precipitation in the JN1 steel aged at 700 °C for 1000 h.

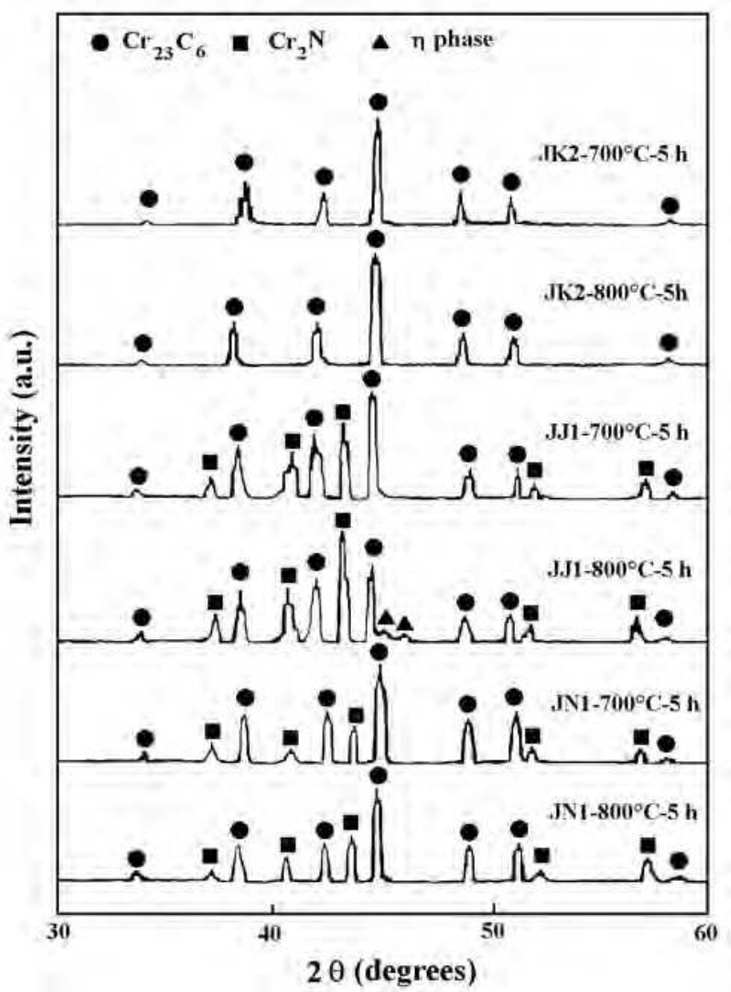

Fig. 7. X-ray diffraction patterns of extracted residues for JN1, JJ1 and JK2 steels agedat 700 and 800 °C for 5 h.

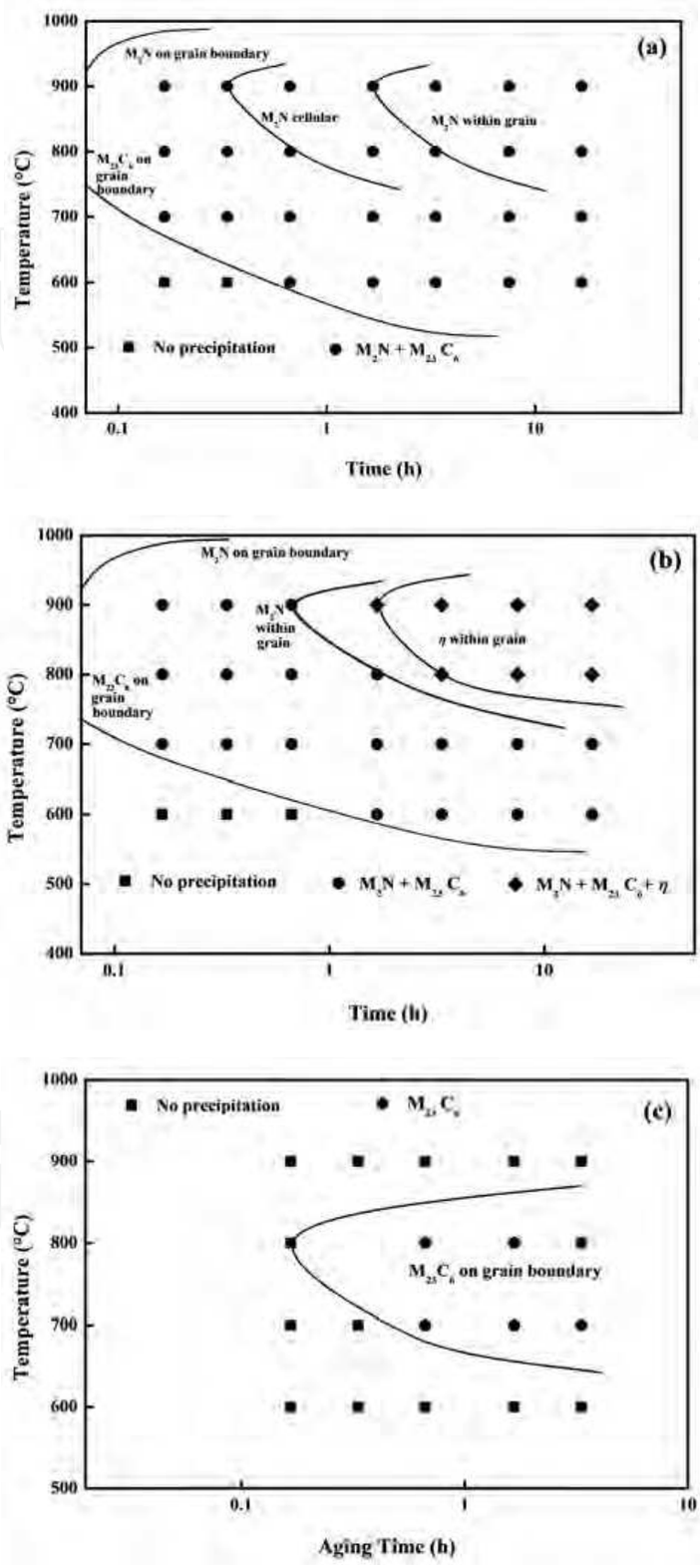

Fig. 8. TTP diagrams of the (a) JN1, (b) JJ1 and (c) JK2 steels.

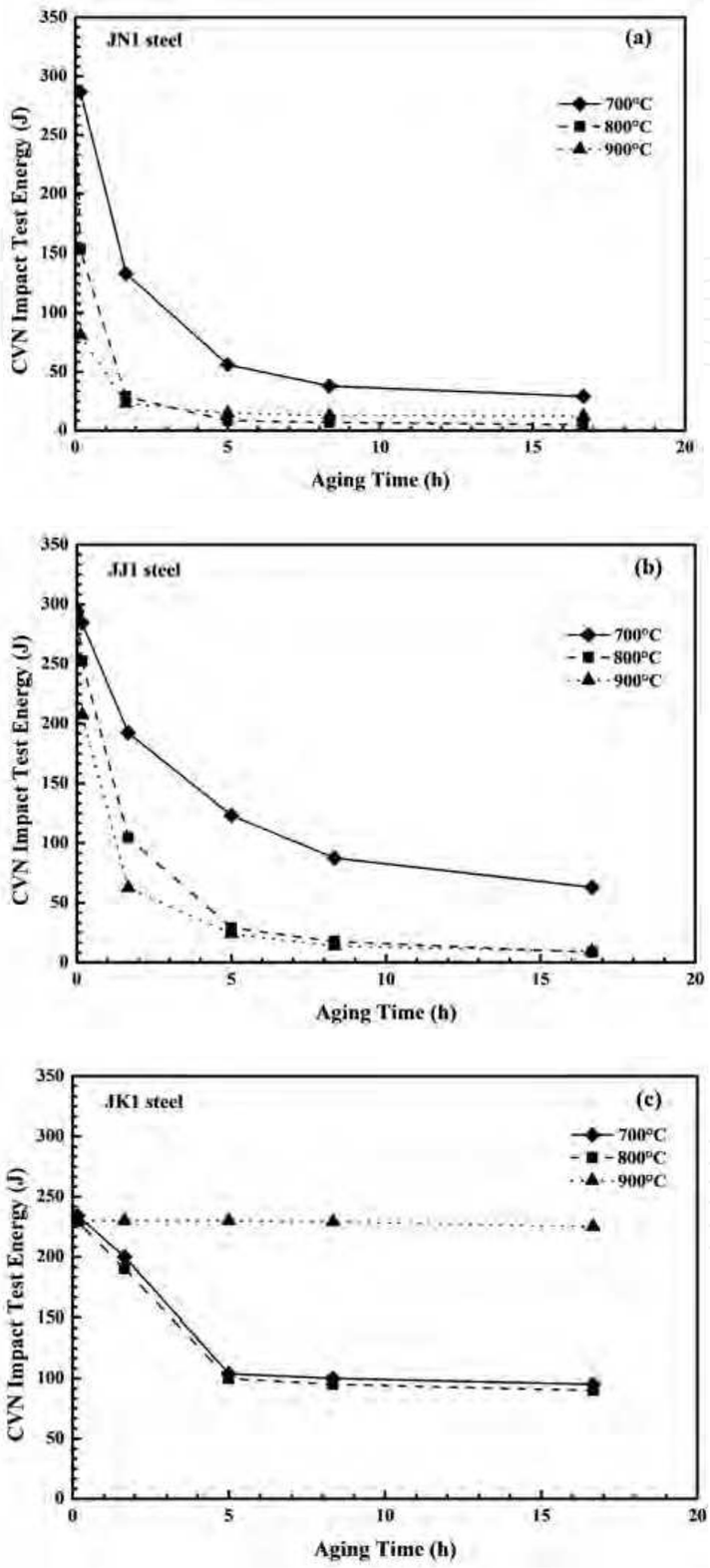

Fig. 9. Plot of CVN impact energy at – 196 °C vs. aging time for tested steels.

2.3 Cellular precipitation in a Mg-8.5Al-0.5Zn-0.2Mn alloy

Mg-Al-Zn alloys have become one of the most important light alloys with a wide range of applications in the automotive industry. This is attributed to the best combination of castability, mechanical strength and ductility (Kainer, 2003). The AZ series of magnesium alloys are mainly based on the Mg-Al binary alloys system. According to the equilibrium Mg-Al alloy phase diagram, the equilibrium phases are the hcp Mg-rich α phase and $Mg_{17}Al_{12}$-γ phase with a complex bcc structure. During the aging process of the Mg-Al based alloys, two types of precipitation are present. That is, discontinuous precipitation takes place on grain boundaries. One of these, intergranular precipitations occurs forming a lamellar structure and it is also known as cellular precipitation. Additionally, continuous precipitation takes place in an intragranular manner and it exhibits more complicated morphologies and orientation relationships than the cellular precipitation. It has been shown in several works (Lai et al., 2008) that these alloys have a poor response to precipitation hardening, compared with precipitation-hardenable Al alloys. Furthermore, the aging hardness is strongly influenced by the morphology, the size and the distribution density of $Mg_{17}Al_{12}$ precipitates. Besides, it has been reported that both discontinuous and continuous precipitations have an effect on the hardness of these alloys (Contreras-Piedras, et al., 2010). Thus, this section shows the mechanism and growth kinetics of cellular precipitation in a Mg-8.5Al-0.5Zn-0.2Mn (wt.%) alloy aged isothermally at 100, 200 and 300 °C for different time periods.

2.3.1 Experimental details

A Mg-8.5Al-0.5Zn-0.2Mn (wt.%) alloy was melted using pure metallic elements under a protective argon atmosphere. Table 1 shows the chemical analysis corresponding to this alloy. Specimens of 10 mm x 10 mm x 10 mm were cut from the ingot and encapsulated in a Pyrex tube under an argon atmosphere. These were homogenized at 430 °C for 3 days and subsequently water-quenched. Homogenized and solution-treated specimens were aged at 100, 200 and 300 °C for different times. The heat-treated specimens were analyzed by X-ray diffraction with copper Kα radiation. These specimens were prepared metallographically and etched with an etchant composed of 19 ml distilled water, 60 ml ethylene glycol, 20 ml glacial acetic acid and 1 ml nitric acid. Etched specimens were observed at 25 kV with a scanning electron microscope equipped with EDS analysis. Vickers hardness was measured in all the heat-treated samples with a load of 100 g. The volume fraction of the discontinuous precipitation was determined from SEM images using a commercial image analyzer.

2.3.2 Microstructural characterization

The X-ray diffraction patterns of the specimens in the conditions of solution-treated and aged at 300 °C for 150 h are shown in Fig. 10. A single-phase is confirmed in the solution-treated specimen, while the appearance of XRD peaks corresponding to the $Mg_{17}Al_{12}$-γ phase are evident in the XRD pattern of the specimen aged at 300 °C for 150 h. No other phases were detected. The presence of these phases for each case is in agreement with the equilibrium Mg-Al phase diagram. Figures 11 (a-i) show the SEM micrographs for the specimens aged at 100, 200 and 300 °C for different time periods. There is a clear competition between the discontinuous and continuous precipitation from the early to the late stages of aging (see, for instance Fig. 11 (e)). Some intragranular precipitates are also

observed in these micrographs, Fig. 11 (h). In general, there is a precipitate coarsening as the aging process progresses, Figs. 11 (e-f) and (h-i). The morphology of cellular precipitation at 100 and 200 °C mainly consisted of an S-shape and double-seam morphologies. In contrast, the shape corresponding to 300 °C was mainly a single-seam. It has been reported (Aaronson et al., 2010) that the first morphology occurs at a low temperature ($T<T_m/2$) and it is associated with the free-boundary mechanism and the second one takes place at lower temperature and it is related to the precipitate-assisted mechanism.

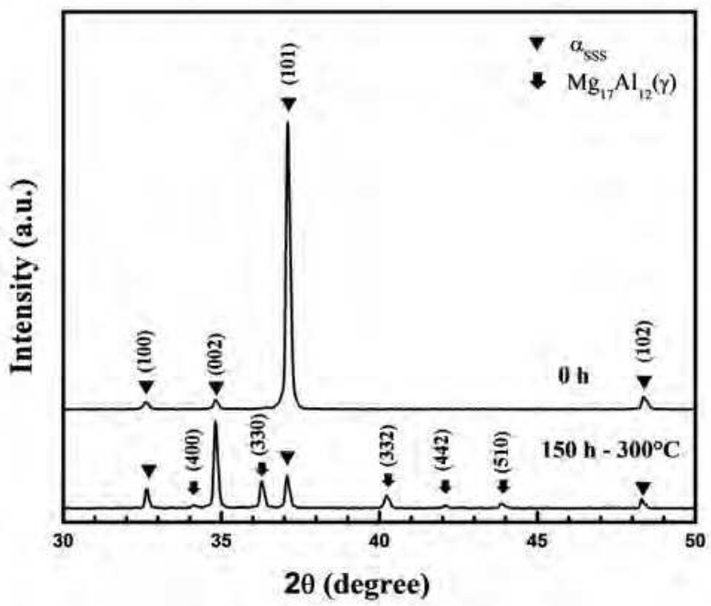

Fig. 10. XRD patterns of the specimens solution-treated and aged at 300 °C for 150 h.

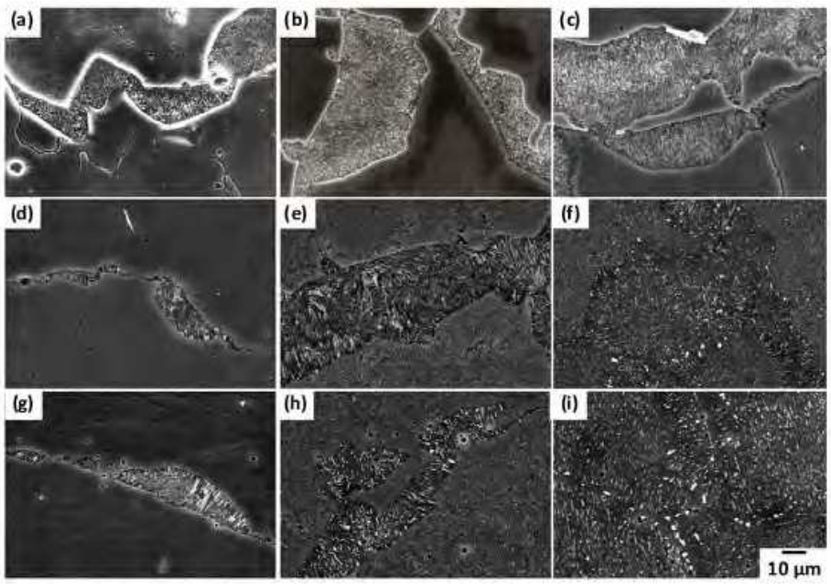

Fig. 11. SEM micrographs of the alloy aged at 100°C for (a) 550, (b) 1500 and (c) 3000 h, At 200 °C for (d) 1, (e) 10 and (f) 250 h, and at 300°C for (g) 0.9, (h) 1 and (i) 25 h.

2.3.3 Growth kinetics of cellular precipitation

The plot of volume fraction of cellular precipitation vs. aging time is shown in Fig. 12. The highest volume fraction occurred for the lowest aging temperature, 100 °C. This fact suggests that continuous precipitation extends more rapidly within grains limiting the growth of cellular precipitation. The analysis of the plot of the volume fraction X_f vs. aging time t, Fig. 12, was carried out using the Johnson-Mehl-Avrami-Kolmogorov equation (Cahn, 1975):

$$X_f = 1 - \exp\left(-kt^n\right) \quad (2)$$

The time exponent n was determined to be about 1.1, 0.85 and 0.87 for 100, 200 and 300 °C, respectively. These exponent values are close to 1 and it is associated with the dimensionality of the saturation site. That is, it corresponds to a boundary (Cahn, 1975). The lamellar structure always nucleates at grain boundaries and grows perpendicularly to them. The cellular growth stops only if the volume fraction of continuous precipitation is significant to impede its growth. In addition, the activation energy for the cellular precipitation was determined to be about 64.6 kJ mol^{-1}. It was obtained by the slope of the straight line in the Arrhenius plot of the time for a volume fraction of 0.6 vs. the reciprocal value of the absolute temperature as shown in Fig. 5. This energy value seems to be reasonable because it is much lower than the self-diffusion of Mg, 135 kJ mol^{-1} (Mehrer, 1990). That is, it seems to correspond to a grain boundary diffusion process. Additionally, an energy value of 84 kJ mol^{-1} was reported for the cellular precipitation in the binary Al-Zn alloy system (Contreras et al., 2010), which is also a low energy value as that found in present work. Figure 6 shows the variation of interlamellar spacing, S, of discontinuous precipitation as a function of temperature. An increase in lamellar spacing is observed with the increase in temperature. A similar behavior was reported for the discontinuous precipitation in Al-Zn alloys (Contreas et al. 2010). According to the Turnbull theory for cell growth kinetics, the interlamellar spacing S is defined as follows (Aaronson et al. 2010):

$$S=-4\gamma V/\Delta G \quad (3)$$

Where γ is the interfacial energy, V the molar volume, and ΔG the free energy associated with the cellular reaction. ΔG has an inverse relation with undercooling, temperature. Thus, the lower temperature corresponds to the shorter interlamellar spacing. Moreover, the interlamellar spacing remains constant with the increase in aging time for all aging temperatures. These facts seem to be in agreement with the Turnbull theory, which predicts constant lamellar spacing and lamellae growth rate according to the following equation (Aaronson et al., 2010):

$$G \approx \sim 4\delta D_\delta / S^2 \quad 4)$$

Where G is the lamellae growth rate, D_b is the solute diffusivity along the cell boundary and δ is the cell boundary thickness.

2.3.4 Hardenin behavior

The aging curves for 100, 200 and 300 °C are shown in Fig. 7. The lowest and fastest hardness peak was observed in the aging at 300 °C. This behavior can be attributed to the

rapid coarsening of the $Mg_{17}Al_{12}$-γ precipitates either in the discontinuous or continuous precipitations. In contrast, the highest and slowest hardness peaks occurred in the alloy aged at 100 °C. This fact seems to be related to the fine continuous precipitation due to the slow diffusion process at this temperature.

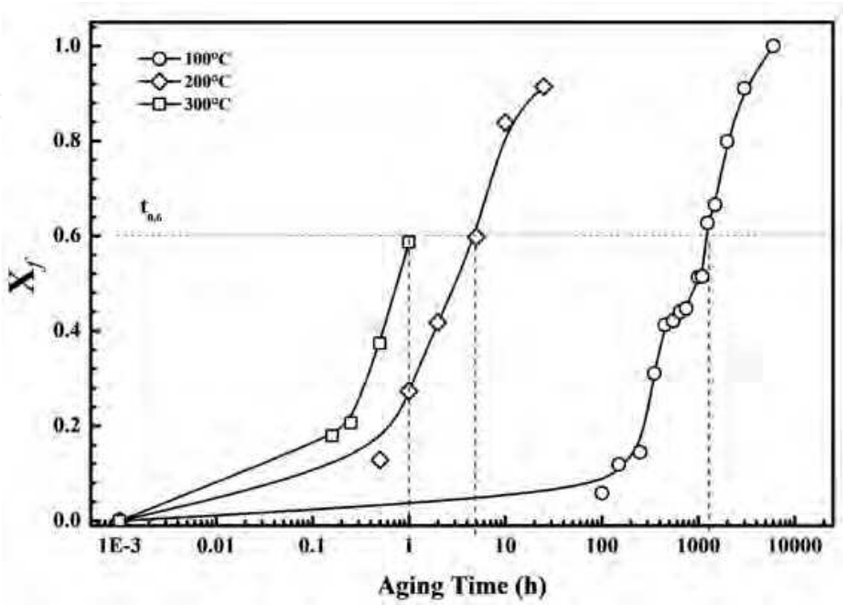

Fig. 12. Volume fraction of cellular precipitation vs. aging time of the alloy aged at 100, 200 and 300 °C.

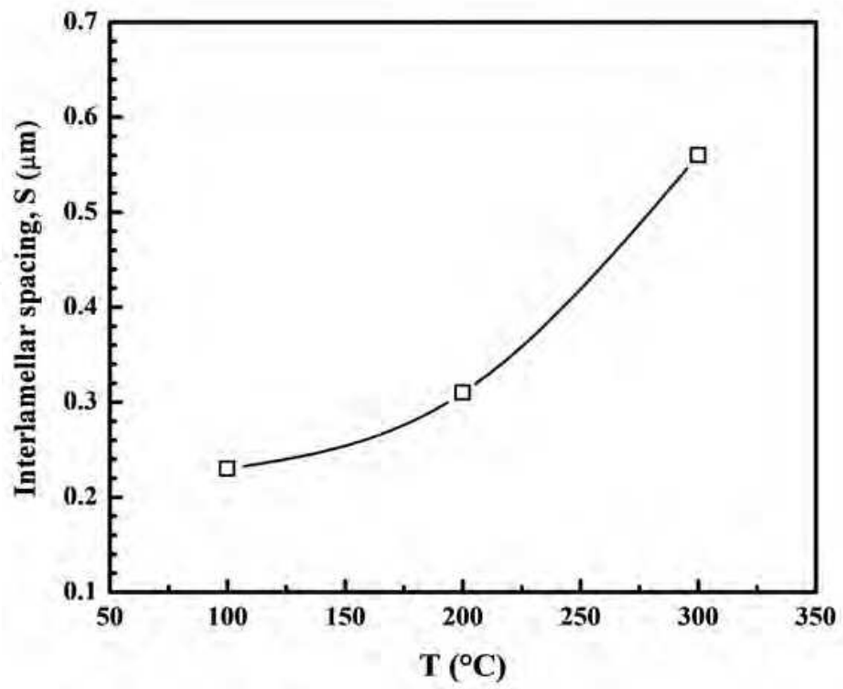

Fig. 13. Interlamellar spacing as a function of aging temperature.

In summary, the microstructural evolution and growth kinetics were studied in an isothermally-aged Mg-8.5Al-0.5Zn-0.2Mn (wt%) alloy and the growth kinetics of cellular precipitation was evaluated using the Johnson-Mehl-Avrami-Kolmogorov equation analysis (Cahn, 1975), which gives a time exponent close to 1. This value confirms that cellular precipitation takes place on the saturation sites corresponding to grain boundaries. Additionally, the activation energy for the cellular precipitation was determined to be about 64.6 kJ mol^{-1}. This also indicates a grain boundary diffusion process. The variation of cellular spacing with temperature follows the behavior expected by Turnbull theory. The highest hardness peak corresponded to the lowest aging temperature and it is associated with a fine continuous precipitation, while the lowest hardness peak was detected at the highest aging temperature and it is attributed to the rapid coarsening process of both precipitations.

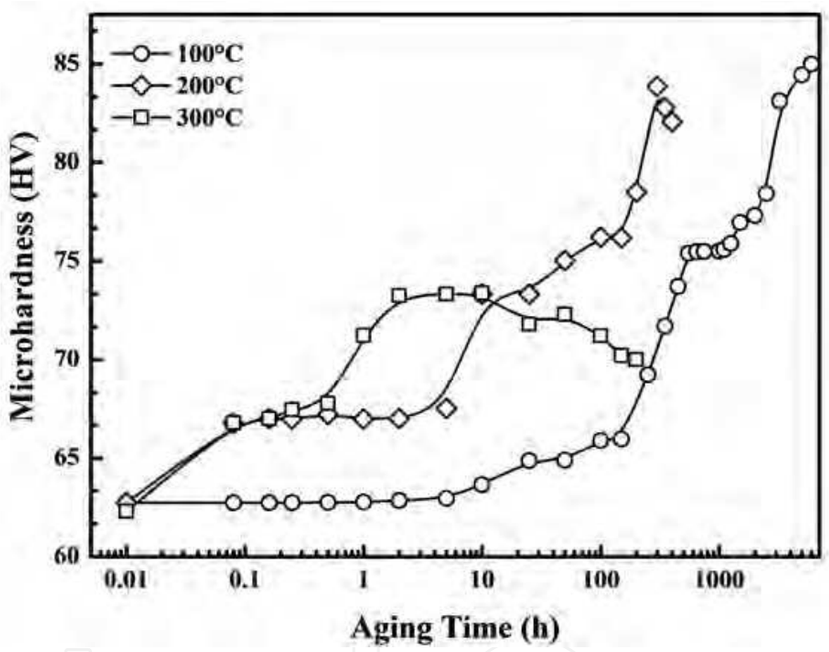

Fig. 14. Aging curves for 100, 200 and 300 °C.

3. Conclusion

This chapter showed three applications of SEM characterization for the analysis of different phase transformations in ferrous and nonferrous alloys, as well as its effect on their mechanical properties. The analysis of these phase transformations enables us to characterize the growth kinetics of these transformations which can be useful either to design heat tretments in order to obtain better mechanical properties or to analyze the microstructural evolution in order to asses the mechanical properties of a component-in-service. Besides, it was shown that the SEM characterization parameters can be used along with the phase transformation theories permitting a better understanding of the transformation behavior in materials after heating.

4. Acknowledgment

The authors wish to acknowledge the financial support from Instituto Politecnico Nacional (ESIQIE), SIP-IPN and CONACYT 100584.

5. References

Aaronson, H.I, Enomoto M. & Lee, J.K. (2010). *Mechanism of Diffusional Phase Transformations in Metals and Alloys*, CRC Press, ISBN 978-1-4200-6299-1, NW, USA

Cayetano-Castro, N.; Dorantes-Rosales H., Lopez-Hirata, V.M., Cruz-Rivera, J. & Gonzalez-Velazquez, J.L. (2008). Cinética de Engrosamiento de Precipitados Coherentes en la Aleación Fe-10%Ni-15%Al. *Revista de Metalurgia de Madrid*, Vol. 44, No. X, (Month, 2008) pp. 162-169, ISSN 1582-2214

Christian J.W. (1975), *The Theory of Transformations in Metals and Alloys*, Pergamon Press, ISBN 0-08-018031-0, Oxford, UK

Contreras-Piedra, E., Esquivel-Gonzalez, R., Lopez-Hirata, V.M., Saucedo-Muñoz, M.L., Paniagua-Mercado, A.M. & Dorantes-Rosales, H.J. (2010). Growth Kinetics of Cellular Precipitation in a Mg-8.5Al-0.5Zn-0.2Mn (wt.%) Alloy, *Materials Science Engineering A*, Vol. 527, pp. 7775-7778, 2010. ISSN 0921-5093

Kainer, K.U. (2003), Magnesium- Alloys and Technologies, Wiley-VCH, ISBN 3-527-30570-X, Germany

Kikuchi M., Kajihara M. & Choi S. (1991). Cellular Precipitation Involving both Substitutional and Interstitial Solutes: Cellular of Cr_2N in Cr-Ni Austenitic Steels. *Materials Science Engineering A*, Vol. 146, pp. 131-150, ISSN 0921-5093

Kostorz, G. (2001). *Phase Transformations in Materials*, Wiley-VCH, ISBN 3-527-30256-5, Weinheim, Germany

Lai W.J.; Lai, Y.Y. Lu, Y.F. Hsu, S. Trong, W.H. Wang. (2009). Aging behaviour and precipitate morphologies in Mg–7.7Al–0.5Zn–0.3Mn (wt.%) alloy, *Journal of Alloys Compounds,* Vol. 476, pp.118-124, ISSN 0925-8388

Marshal, P. (1984). *Austenitic Stainless Steels Microstructure and Properties*, Elsevier Applied Science Publisher, ISBN 0267-0836, NY, USA

Mehrer, H. (1990), *Numerical Data and Functional Relationship in Science and Technology*, Landolt-Borstein New Series III/26, ISBN 0-387-50886-4, Springer-Verlag, Berlin, Germany

Nakajima H., Nunoya Y., Nozawa M., Ivano O., Takano K., Ando S. & Ohkita S. (1996). Development of High Strength Austenitic Stainless Steel for Conduit of Nb_3Al Conductor, *Advances in Cryogenic Engineering*, Vol. 42 A, pp. 323-330, ISSN 0065-2482

Porter D.A.; Easterling, K.E. & Sherif, M.Y (2009). *Phase Transformations in Metals and Alloys*, CRC Press, ISBN 978-1-4200-6210-6, NW, USA.

Ratke, L. & Vorhees, P.W. (2002). *Growth and Coarsening: Ripening in Materials*, Springer, Berlin, Germany, ISBN 3-540—42563-2

Sauthoff, G. (1995). *Intermetallics,* Wiley-VCH, ISBN 3-527-29320-5, Weinheim, Germany

Soriano-Vargas, O.; Saucedo-Muñoz, M.L., Lopez-Hirata, V.M. & Paniagua Mercado, A. (2010). Coarsening of β´ Precipitates in an Isothermally-Aged Fe_{75}-Ni_{10}-Al_{15} Alloy, *Mater. Trans. JIM*, Vol. 51, No. x, (Month, 2010), pp.442-446, ISSN 1345-9678

Saucedo-Muñoz, M.L.;, Watanabe Y., Shoji T. & Takahashi H. (2001), Effect of Microstructure Evolution on Fracture Toughness in Isothermally Aged Austenitic Stainless Steels for Cryogenic Applications. *Journal of Cryogenic Materials*, Vol. 40, pp. 693-700. ISSN 011-2275

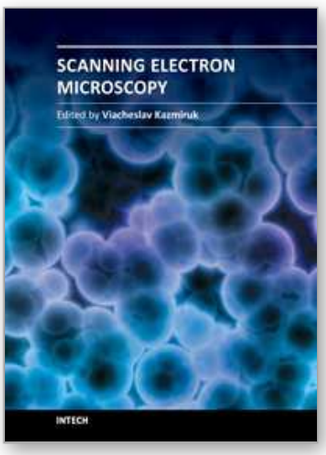

Scanning Electron Microscopy

Edited by Dr. Viacheslav Kazmiruk

ISBN 978-953-51-0092-8
Hard cover, 830 pages
Publisher InTech
Published online 09, March, 2012
Published in print edition March, 2012

Today, an individual would be hard-pressed to find any science field that does not employ methods and instruments based on the use of fine focused electron and ion beams. Well instrumented and supplemented with advanced methods and techniques, SEMs provide possibilities not only of surface imaging but quantitative measurement of object topologies, local electrophysical characteristics of semiconductor structures and performing elemental analysis. Moreover, a fine focused e-beam is widely used for the creation of micro and nanostructures. The book's approach covers both theoretical and practical issues related to scanning electron microscopy. The book has 41 chapters, divided into six sections: Instrumentation, Methodology, Biology, Medicine, Material Science, Nanostructured Materials for Electronic Industry, Thin Films, Membranes, Ceramic, Geoscience, and Mineralogy. Each chapter, written by different authors, is a complete work which presupposes that readers have some background knowledge on the subject.

INTECH
open science | open minds

InTech Europe
University Campus STeP Ri
Slavka Krautzeka 83/A
51000 Rijeka, Croatia
Phone: +385 (51) 770 447
Fax: +385 (51) 686 166
www.intechopen.com

InTech China
Unit 405, Office Block, Hotel Equatorial Shanghai
No.65, Yan An Road (West), Shanghai, 200040, China
中国上海市延安西路65号上海国际贵都大饭店办公楼405单元
Phone: +86-21-62489820
Fax: +86-21-62489821

IntechOpen